

# Implementing an electronic sideband offset lock for precision spectroscopy in radium

T. RABGA,<sup>1,2,3,\*</sup> K. G. BAILEY,<sup>1</sup> M. BISHOF,<sup>1,†</sup> D. W. BOOTH,<sup>1</sup> M. R. DIETRICH,<sup>1</sup> J. P. GREENE,<sup>1</sup> P. MUELLER,<sup>1</sup> T. P. O'CONNOR,<sup>1</sup> AND J. T. SINGH<sup>2</sup>

<sup>1</sup>Physics Division, Argonne National Laboratory, Argonne, Illinois 60439, USA

<sup>2</sup>National Superconducting Cyclotron Laboratory and Department of Physics and Astronomy, Michigan State University, East Lansing, Michigan 48824, USA

<sup>3</sup>Currently with the Center for Correlated Electron Systems, Institute for Basic Science (IBS) and Department of Physics and Astronomy, Seoul National University (SNU), Seoul 151-742, Republic of Korea

\*[trabga@snu.ac.kr](mailto:trabga@snu.ac.kr)

†[bishof@anl.gov](mailto:bishof@anl.gov)

**Abstract:** We demonstrate laser frequency stabilization with at least 6 GHz of offset tunability using an in-phase/quadrature (IQ) modulator to generate electronic sidebands (ESB) on a titanium sapphire laser at 714 nm and we apply this technique to the precision spectroscopy of  $^{226}\text{Ra}$  and  $^{225}\text{Ra}$ . By locking the laser to a single resonance of a high finesse optical cavity and adjusting the lock offset, we determine the frequency difference between the magneto-optical trap (MOT) transitions in the two isotopes to be  $2630.0 \pm 0.3$  MHz, a factor of 29 more precise than the previously available data. Using the known value of the hyperfine splitting of the  $^3P_1$  level, we calculate the isotope shift for the  $^1S_0$  to  $^3P_1$  transition to be  $2267.0 \pm 2.2$  MHz, which is a factor of 8 more precise than the best available value. Our technique could be applied to countless other atomic systems to provide unprecedented precision in isotope shift spectroscopy and other relative frequency comparisons.

© 2023 Optical Society of America under the terms of the [OSA Open Access Publishing Agreement](#)

## 1. Motivation and Background

Laser frequency stabilization techniques are ubiquitous in applications such as precision spectroscopy [1], laser cooling and trapping of atoms [2] and molecules [3], and quantum information science [4]. Laser frequency stabilization is often achieved via comparison to a stable frequency reference. The most common frequency references include optical cavities and atomic or molecular transitions, but any system with a stable, measurable, and selective response to laser frequency can be used. This response signal, can then be used as an "error signal," which tracks the laser's frequency deviations from the stable reference and can be "fed back" to parameters that control the laser frequency to cancel these deviations. In this work, we use the reflection signal from a high-finesse optical cavity near a cavity resonance as our frequency reference.

In a side-of-peak locking scheme, one locks the laser frequency to the side of an optical cavity resonance - using the slope of the cavity resonance as the error signal. Although this allows some tunability in the frequency of the laser, by selecting different positions on the resonance, it couples any laser intensity fluctuations to its frequency instability. A preferred and an improved method uses the Pound-Drever-Hall (PDH) locking scheme [5, 6]. This involves the phase modulation of the laser beam incident on a optical cavity reference. The reflected signal off of the cavity is collected on to a photo detector and demodulated to generate the error signal. This method overcomes the sensitivity to intensity fluctuations from the side-of-peak scheme at the price of tunability, since insensitivity to laser intensity noise is optimal only on the resonance peak.

However, it is still often desirable to have a tunable laser frequency lock while maintaining frequency stability. There are a variety of ways to achieve this goal. Using an acousto-optic

modulator (AOM), one can achieve several hundreds of MHz of frequency tunability [7]. Alternatively an offset phase lock to another frequency stabilized laser can achieve tunable frequency locks over a larger tuning range [8], but requires an additional laser. The electronic side-band (ESB) offset lock, a simple extension to the PDH lock, allows laser frequency stabilization to a fixed frequency reference with a broadly tunable offset frequency [9, 10]. Offset frequencies up to 4 GHz have been achieved by combining the ESB offset locking technique with a high-bandwidth, fiber-coupled electro-optical modulator (EOM) [11]. Here, we describe the methods used to implement an ESB offset lock for laser frequency stabilization with an offset frequency that is tunable between 200 MHz and 6 GHz. In contrast to previous work, we use an in-phase/quadrature (IQ) modulator (Analog Devices, LTC5588-1) to generate the laser modulation signal from inexpensive digital signal generators. This eliminates the need for expensive microwave signal generators capable of carrier phase modulation at several MHz. Moreover, our approach can be adapted to a greater number of applications owing to the broad availability of low cost synthesizers and IQ modulators across the entire RF and Microwave spectrum. We leverage our ESB offset lock to perform laser spectroscopy of radium isotopes and compare the frequencies of different atomic transitions to the same optical cavity resonance. We determine the frequency difference between isotopes with precision and accuracy limited only by the cavity resonance, lock implementation, and fundamental atomic properties.

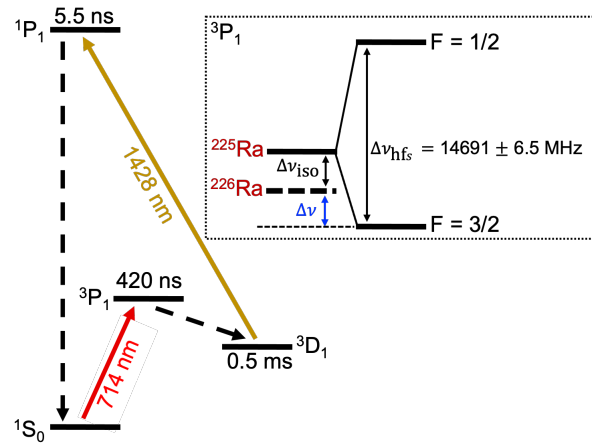


Fig. 1. The atom slowing and cooling scheme used to trap  $^{226}\text{Ra}$  and  $^{225}\text{Ra}$  in a MOT. The  $1S_0 \rightarrow 3P_1$  transition requires a single repump laser at 1428 nm to excite the  $3D_1 \rightarrow 1P_1$  transition and close the cooling cycle. Inset: The frequency difference  $\Delta\nu$  between the MOT transitions for the two isotopes is shown. Also shown are the isotope shift for the transition  $\Delta\nu_{\text{iso}}$  and the hyperfine splitting  $\Delta\nu_{\text{hfs}}$  in  $^{225}\text{Ra}$ .

Spectroscopy of radium isotopes is of extreme importance due to their unique atomic and nuclear properties that make them suitable for electric dipole moment (EDM) searches. A non-zero EDM in a non-degenerate system violates time-reversal (T) symmetry and consequently charge-parity (CP) symmetry [12]. The octupole deformation and nearly degenerate nuclear parity doublet in radium make it an ideal candidate for probing CP violations due to the atomic nucleus [13–16]. The radium EDM experiment at the Argonne National Laboratory uses  $^{225}\text{Ra}$  ( $I = 1/2$ ,  $\tau_{1/2} = 14.9$  day) (where  $I$  is the nuclear spin) to set the best limit on the size of the EDM in  $^{225}\text{Ra}$  [17]. Its 14.9-day half-life and low vapor pressure make  $^{225}\text{Ra}$  a challenging system for an EDM experiment. Due to its greater abundance and longer half-life,  $^{226}\text{Ra}$  ( $I = 0$ ,  $\tau_{1/2} = 1600$  yr) is used to optimize certain parts of the EDM experimental apparatus, such as the atom cooling and trapping setup. Therefore it is crucial to be able to quickly and reliably

tune laser frequencies over several GHz in order to laser cool and trap both isotopes. The laser frequency stabilization technique described here provides a convenient and robust method for tuning the laser frequency to the relevant atomic transitions used for cooling and trapping these two isotopes during a single experiment.

The relevant energy levels for slowing and trapping of a radium magneto-optical trap (MOT) are shown in Figure 1 [17]. We perform an improved measurement of the frequency difference  $\Delta\nu$  between the MOT transitions for  $^{226}\text{Ra}$  ( $^1S_0 \rightarrow ^3P_1$ ) and  $^{225}\text{Ra}$  ( $^1S_0 [F=1/2] \rightarrow ^3P_1 [F=3/2]$ ). From the measured  $\Delta\nu$  and the known value for the hyperfine splitting  $\Delta\nu_{\text{hfs}}$  between the  $F = 3/2$  and  $F = 1/2$  levels of  $^3P_1$ , we extract the isotope shift  $\Delta\nu_{\text{iso}}$  between  $^{226}\text{Ra}$  and  $^{225}\text{Ra}$  for the  $^1S_0 \rightarrow ^3P_1$  transition.

## 2. Implementing an ESB Offset Lock Using an IQ Modulator

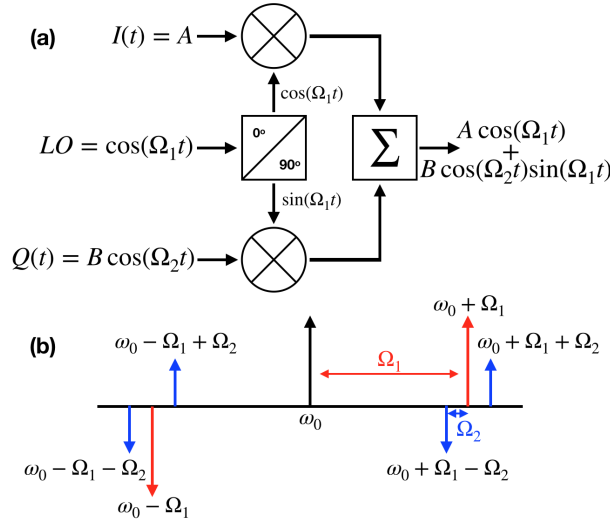


Fig. 2. (a) A schematic showing the generation of sidebands using an IQ modulator. An RF signal at  $\Omega_1$  fed into the LO port is split into the in-phase and quadrature components. The quadrature part is modulated with an RF signal at  $\Omega_2$  and combined with the in-phase component. (b) The frequency sidebands created on an input laser frequency at  $\omega_0$  by the IQ modulated EOM up to  $\mathcal{O}(J_1)$  in Eq. 2.

An IQ modulator splits the input carrier radiofrequency signal into its In-phase (I) and Quadrature (Q) components. With appropriate choices of inputs into the I and Q ports it can approximate frequency modulation. In our case, to generate the necessary frequency sidebands, a carrier with frequency  $\Omega_1$  is fed into the local oscillator (LO) port of the IQ modulator. A constant DC voltage is fed into the I port while a modulation signal with frequency  $\Omega_2$  is fed into the Q port. The resultant combination of the in-phase and quadrature signals is then applied to the EOM. The principle of operation of an IQ modulator is shown in Figure 2a.

The electric field of a laser beam with frequency  $\omega_0$  and amplitude  $E_0$  can be written as

$$E(t) = E_0 e^{i\omega_0 t} \quad (1)$$

For the ESB offset lock scheme, the IQ modulated signal  $A \cos(\Omega_1 t) + B \cos(\Omega_2 t) \sin(\Omega_1 t)$  is amplified and applied to the EOM. The modulated electric field of the laser beam is then given by

$$E(t) = E_0 e^{i\{\omega_0 t + A \cos(\Omega_1 t) + B \cos(\Omega_2 t) \sin(\Omega_1 t)\}} \quad (2)$$

where,  $\Omega_1$  and  $\Omega_2$  are the respective modulations into the LO and the Q ports of the IQ modulator with associated modulation depths  $A$  and  $B$  respectively. Expanding the above expression in terms of Bessel functions, with terms up to  $O(J_1^2)$ , enables us to see the associated sidebands generated.

$$E(t) \approx E_0 \left\{ J_0(A) J_0^2(B/2) e^{i\omega_0 t} + i J_0^2(B/2) J_1(A) \left[ e^{i(\omega_0 + \Omega_1)t} + e^{i(\omega_0 - \Omega_1)t} \right] \right. \quad (3a)$$

$$+ J_0(A) J_1^2(B/2) \left[ e^{i(\omega_0 + 2\Omega_1)t} + e^{i(\omega_0 - 2\Omega_1)t} - e^{i(\omega_0 + 2\Omega_2)t} - e^{i(\omega_0 - 2\Omega_2)t} \right] \quad (3b)$$

$$+ J_0(B/2) J_1(B/2) (J_0(A) - 2J_1(A) \sin(\Omega_1 t)) \times \left[ e^{i(\omega_0 + \Omega_1 - \Omega_2)t} + e^{i(\omega_0 + \Omega_1 + \Omega_2)t} - e^{i(\omega_0 - \Omega_1 + \Omega_2)t} - e^{i(\omega_0 - \Omega_1 - \Omega_2)t} \right] \left. \right\} \quad (3c)$$

where  $J_n$  is the  $n$ -th order Bessel function of the first kind. Up to terms linear in  $J_1$ , we see the six sidebands generated as shown in Figure 2b. We also note in Eq. 3c, that in terms up to  $O(J_1^2)$  we observe amplitude modulations at  $\Omega_1$ . This is a consequence of using an IQ modulator for phase-modulations, there is always some amplitude modulation. For the present purposes, we focus our attention on the modulation at  $\omega_0 - \Omega_1$  and the two sidebands generated at  $\omega_0 - \Omega_1 - \Omega_2$  and  $\omega_0 - \Omega_1 + \Omega_2$ . This is similar to the sidebands generated for the PDH scheme. The modulation at  $\Omega_2$  generates the error signal, while the modulation at  $\Omega_1$  provides the tunability of the lock. Compared to a conventional phase-modulated PDH frequency stabilization scheme with a modulation at frequency  $\Omega_1$  with a modulation-depth  $A$ , the relative size of the error signal (up to  $O(J_1^2)$ ) is given by

$$D_{\text{ESB}}/D_{\text{PDH}} = J_0^3(B/2) J_1(B/2) \left[ 1 - \frac{2J_1(A)}{J_0(A)} \sin(\Omega_1 t) \right] \quad (4)$$

By tuning the EOM offset frequency  $\Omega_1$  we change the offset of the laser frequency from the resonant optical cavity mode and therefore tune the laser frequency. The collision of the different sidebands as one tunes  $\Omega_1$  poses a potential issue for broadband applications. In the above case, when  $\Omega_1$  is a multiple of  $\Delta\nu_{\text{FSR}}/2$ , where  $\Delta\nu_{\text{FSR}}$  is the free spectral range of the optical cavity, we notice the collision of the sidebands with opposite phases at  $\omega_0 + \Omega_1$  and  $\omega_0 - \Omega_1$ . This can significantly affect the error signal and therefore the lock performance. However, we find that adding an AOM in the pathway helps optimize the tuning frequency  $\Omega_1$  and, as a result, prevents any lock degradation (See Fig 5). Incidentally, this effect can also be used to conveniently and accurately measure  $\Delta\nu_{\text{FSR}}$  of the cavity. One can tune the laser so that it scans a range near the center of two  $\text{TEM}_{00}$  modes, then adjust  $\Omega_1$  until the error signal of the lower frequency mode precisely cancels that of the higher order mode. The free spectral range is then twice  $\Omega_1$ . Greater relative accuracy can be obtained by comparing non-adjacent modes, and measuring 4 or 5 times  $\Delta\nu_{\text{FSR}}$ .

### 3. Characterizing the ESB Offset Lock Performance

To characterize lock performance, we implement an ESB offset lock to an optical cavity using a 483 nm external cavity diode laser (ECDL1, Toptica DL Pro) and analyze the optical beat note between ECDL1 and a similar, unstabilized 483 nm laser (ECDL2, Moglabs CEL). The experimental setup is shown in Fig 3.

#### 3.1. ESB Offset Lock Test Setup

A portion of the 483 nm ECDL1 laser power is modulated by a fiber coupled EOM (AdvR, KTP phase modulator), and sent to an optical reference cavity made from a zerodur spacer and fused

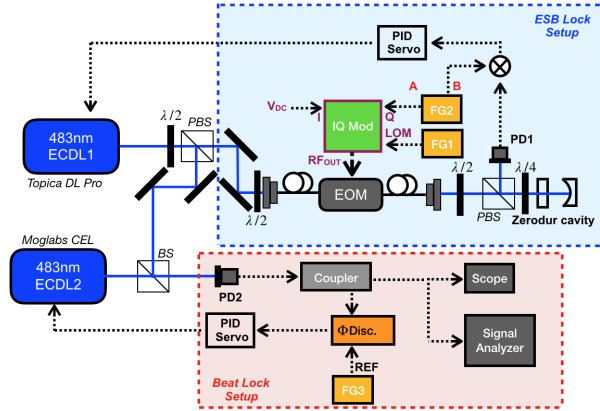


Fig. 3. The blue shaded region shows the ESB offset lock setup for ECDL1. Modulation of the laser light incident on the zerodur optical cavity is provided by an IQ modulator-driven EOM. Two separate function generators (FG1 and FG2) provide the signals for the local oscillator input (LOM) and the quadrature modulation input (Q) respectively. The resultant reflected light from the optical cavity is collected on the photo detector (PD1) and the signal demodulated and input to a PID controller which outputs to ECDL1 diode current and external cavity piezo voltage for frequency stabilization. Shown in the red shaded region is the optical beat-lock setup for frequency stabilization of ECDL2. The optical beat signal is collected on a photo detector (PD2) and sent to a phase discriminator ( $\Phi$ Disc.) which compares it against a reference frequency from a function generator (FG3). The output is sent to a PID controller which outputs to the diode current and piezo voltage of ECDL2. The reference frequency determines the frequency offset between the two lasers, however, the beat lock feedback is not engaged while the optical beat is used to evaluate the ESB offset lock.

silica high-reflectivity mirrors. The IQ modulation scheme for generating sidebands and locking the laser frequency is identical to what is described later in section 4.1. For ECDL1 we feedback on the DC component of the laser current to stabilize its frequency. The optical beat pattern between ECDL1 and ECDL2 is collected on a photo detector (PD2). The beat pattern is sampled and monitored on a signal analyzer and an oscilloscope. Typically, we use the optical beat signal from PD2 to stabilize the frequency of ECDL2 relative to ECDL1 using a phase discriminator and reference frequency (See Fig 3.). To evaluate the ESB lock performance we disengage the feedback on ECDL2 and tune its free-running frequency to achieve an optical beat signal at 100 MHz. This signal is down converted to 20 kHz by mixing the beat pattern with a function generator output at 99.98 MHz.

To test the performance of the ESB offset locking scheme, we compare it to a traditional PDH lock. For the PDH lock, we simply bypass the EOM and send the laser beam straight to the cavity. The AC component of the laser current for ECDL1 is dithered to generate the frequency sidebands. The cavity reflection signal is demodulated to generate the PDH error signal, which is then low-pass filtered and fed to the same PID controller (SRS, SIM960) as for the ESB offset lock.

### 3.2. Lock Evaluation and Optimization

Figure 4 shows the power spectral density (PSD) of the beat pattern normalized to the 20kHz carrier signal, estimated using Welch's method [18]. We calculate the PSD from a 100 ms observation of the beat signal with a 1.25 Mhz sampling rate both when ECDL1 is locked using a traditional PDH lock (black) and using the ESB offset lock (blue). We note that the full width

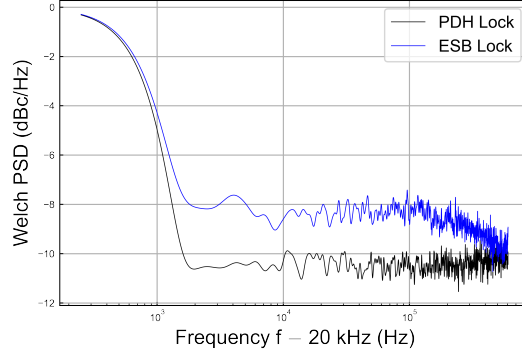


Fig. 4. Beat pattern power spectral density (PSD) for the ESB offset lock and the PDH lock. The optical beat pattern at 100 MHz is collected on a fast photo-detector PD2 and down converted to 20kHz to study the sub-MHz noise in our laser locks. The beat pattern is observed over 100 ms with a sample rate of 1.25 MHz. The Y-axis is the PSD in the signal normalized with respect to the carrier. The X-axis shows the signal frequency offset with respect to the carrier at 20 kHz.

at half maximum of the 20kHz carrier signal is not significantly different between the PDH and ESB locked signals and the small difference in carrier normalized noise above 1kHz is likely due to additional electronic noise in the lock feedback owing to a reduction in optical power coupled to the cavity resonance when the EOM is in use. An additional source of noise in the lock is residual amplitude modulation (RAM) which depends on the temperature of the EOM and the polarization of light sent through the EOM. For this work the EOMs are thermally stabilized and light polarization is adjusted to minimize RAM on the EOM output. We expect that by sending additional optical power through the EOM and active RAM stabilization [19], relative noise on the ESB lock beat signal could be reduced to that of the PDH signal. Still, it is important to note that certain EOMs, such as the one used in our 714 nm ESB lock, are susceptible to significant photo refractive damage when exposed to optical input power above certain thresholds, so the total optical power sent through an EOM may be limited. For this work, the input power is set below the threshold (6 mW) where the photo refractive effect occurs.

We do not expect that additional noise from the ESB-locked ECDL1 will affect atomic spectroscopy on the  $^1S_0$  to  $^1P_1$  transition, which has a natural linewidth of 30 MHz, although it has not yet been tested. We have, however, implemented a very similar ESB cavity lock in our 714 nm laser system (described below) which addresses the  $^1S_0$  to  $^3P_1$  transition. Despite this transition having a natural linewidth that is only 380 kHz, we do not observe any significant difference in the efficiency with which we cool, slow, and trap atoms in a MOT compared to a previous locking scheme which utilized a high-frequency AOM and a traditional PHD lock. Moreover, the estimated 714 nm laser linewidth is consistently observed to be  $\sim 70$  kHz using either locking scheme by comparing the locked error signal fluctuations to the cavity linewidth.

#### 4. MOT Cutoff and Isotope Shift Measurements in $^{225}\text{Ra}$ and $^{226}\text{Ra}$

The following section describes the implementation of an ESB offset lock in our 714 nm laser system and its application to precision spectroscopy in  $^{226}\text{Ra}$  and  $^{225}\text{Ra}$ .

#### 4.1. ESB Offset Lock Setup

The experimental setup used for the ESB offset lock of our 714 nm laser and the MOT cutoff frequency measurements is shown in Fig 5. We generate  $\sim 1.3$  W of 714 nm light from a Ti:Sapphire ring cavity laser (Sirah, Matisse) pumped by a diode-pumped solid state (DPSS) laser (Lighthouse Photonics, Sprout). Most of the light is sent to our laser slowing and trapping setup for radium. A small sample of  $\sim 4$  mW is sent to a fiber-coupled EOM (EOSpace). The EOM provides phase modulation to the laser beam which is sent to an ultra low expansion (ULE) optical cavity for frequency stabilization.

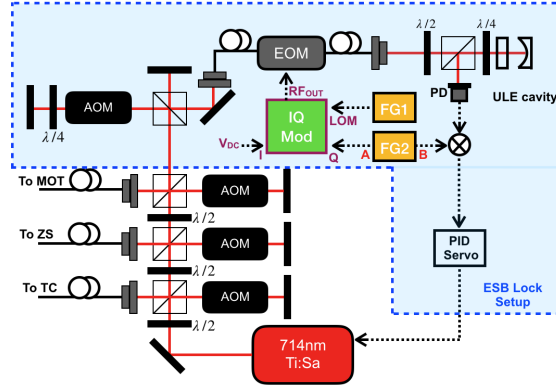


Fig. 5. ESB Lock setup for our 714 nm Ti:Sa ring cavity laser. The laser output power is divided amongst the transverse cooling (TC), Zeeman slower (ZS), MOT, and ESB lock setup. The EOM is driven with the output of the IQ modulator that modulates the laser beam incident on the ULE reference cavity. The components are similar to what is described in Figure 3. The AOM before the EOM input fiber allows us to avoid cavity mode collisions as described in Section 2.

The modulation RF signal is generated by an IQ modulator (Analog Devices, LTC5588-1). A schematic of the IQ modulator is shown in Figure 6 along with the relevant ports and inputs. The blue trace in Figure 7 shows a typical output from the IQ modulator. Here we see the offset sideband at 1 GHz ( $\Omega_1$ ) and the corresponding modulation sidebands that are offset  $\pm 10$  MHz ( $\Omega_2$ ) from  $\Omega_1$ . The reflected light from the cavity is collected on a fast photodiode (PD). The signal is sent to a mixer and demodulated at 10 MHz to create an error signal as shown by the black trace in Figure 7.

The error signal is low-pass filtered and sent to a PID controller inside the Ti:Sapphire laser control box, which feeds back on the fast etalon in the ring cavity to lock the laser frequency to a  $\text{TEM}_{00}$  mode of the ULE cavity. The laser linewidth, when locked, is typically measured to be  $\sim 70$  kHz, limited by the bandwidth of the laser controller.

#### 4.2. MOT Cutoff Measurement Setup

Most of the 714 nm laser power is sent to the transverse cooling (TC) chamber to collimate the atomic beam coming out of the oven, followed by the Zeeman slower (ZS) to slow the longitudinal velocity of the atomic beam below the MOT capture velocity, and finally to the MOT to trap the radium atoms. More details about the experimental design and the slowing and trapping of radium can be found in Ref. [17] The frequency applied to the acousto-optic modulator (AOM) for the MOT beams is switched between a loading and a probe phase using an RF switch. An experimental cycle is set to a total of 25 seconds during which the probe phase lasts for 300 ms, which is the camera exposure time. During the loading phase, the MOT laser frequency is

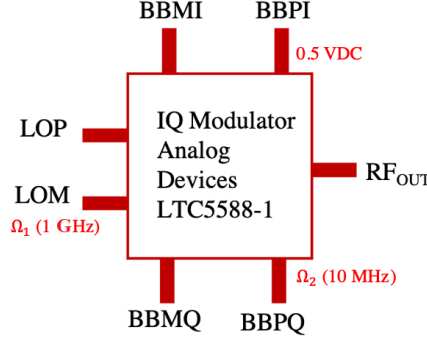


Fig. 6. IQ modulator (Analog Devices, LTC5588-1) with the relevant ports and inputs are shown. The  $\Omega_1$  modulation (1GHz, 0.5Vpp) is fed into the LOM (negative LO input) port of the IQ modulator and the LOP (positive LO input) port is terminated at  $50\ \Omega$ . A constant 0.5 VDC is applied to the BBPI input port of the I-channel of the IQ modulator, and the BBMI port is terminated at  $50\ \Omega$ . The  $\Omega_2$  modulation (FG2) (10 MHz, 0.5 Vpp) is fed into the BBPQ port of the Q-channel of the IQ modulator, and the BBMQ port is DC biased so as to maintain a common mode voltage of 0.5 VDC. The resultant modulation through the  $RF_{OUT}$  port is sent to the EOM.

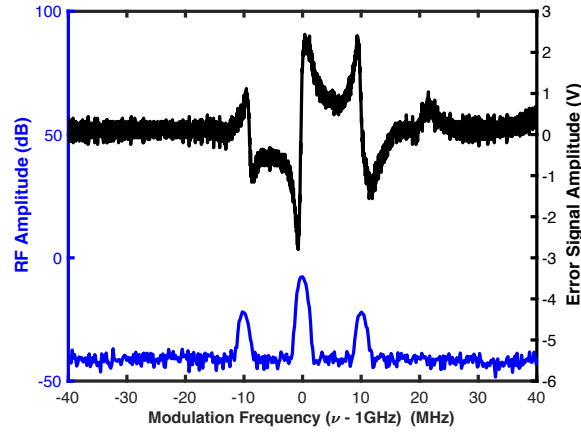


Fig. 7. Blue Trace: Output of the IQ modulator showing the modulation sideband at  $\Omega_1$  with the two sidebands at  $\Omega_1 \pm \Omega_2$ .  $\Omega_1$  is set to 1 GHz and  $\Omega_2$  to 10 MHz. Black Trace: The error signal generated after demodulating the reflected optical signal at  $\Omega_2$ .

red-detuned from resonance by  $8\Gamma$  ( $\Gamma = 2\pi \times 380$  kHz). During the probe phase, we measure the MOT fluorescence on an EMCCD camera (Andor, Luca) for different RF frequencies applied to the MOT AOM.

For  $^{225}\text{Ra}$ , we further offset the laser frequency from the cavity reference mode by 2629.95 MHz. This is achieved by increasing the offset frequency  $\Omega_1$  by the same amount. This highlights the broadband tunability of this implementation of the ESB lock. Locking to the same cavity resonance, we simply increase the laser frequency offset to probe transitions that are several GHz apart. Using the same cavity resonance eliminates any potential systematic or statistical frequency uncertainties introduced by referencing the laser to different cavity resonances.



### 4.3. Data Analysis

We measure the MOT fluorescence signal for  $^{225}\text{Ra}$  and  $^{226}\text{Ra}$  during the probe phase. For each isotope, we collect 5 background images before and after the frequency scan. We scan the MOT probe frequency in steps of 20 kHz to 50 kHz by scanning the RF drive frequency of the MOT AOM during the probe phase. At each frequency step during the scan, we acquire an atom fluorescence image. The atom images are background subtracted to extract the atom fluorescence count.

The MOT cutoff frequency is defined as the laser frequency at which the MOT fluorescence vanishes as frequency is increased. As depicted in Figure 8a, above a certain frequency MOT fluorescence counts drop below the background level. More commonly, isotopic frequency differences in atomic vapors are measured without externally applied fields either in an effusive beam or, for MOT-trapped atoms, the anti-Helmholtz B-field is turned off before probing the freely expanding cloud. Due to the small number of  $^{225}\text{Ra}$  atoms and the weakness of the transition, we require atoms remain trapped to scatter enough photons for detection. Not only have we observed in several elements and isotopes that the MOT cutoff frequency is an accurate, repeatable, and environmentally insensitive absolute frequency reference, but we also demonstrate the insensitivity of this value to key systematic effects below.

To determine the MOT cutoff frequency, we assume the fluorescence signal is linear in the region of the cutoff and fit to the following function the segment of the MOT fluorescence curve containing several data points just before the fluorescence curve plateaus:

$$y(\nu) = \text{Max} [a_1(\nu - a_2), a_1(a_3 - a_2)] \quad (5)$$

This fit function is the maximum between a line with a slope  $a_1$  & x-intercept  $a_2$  and a line with a constant y-intercept given by  $a_1(a_3 - a_2)$ . The MOT cutoff frequency, represented by  $a_3$ , is defined as the frequency at which these two lines intersect. The linear approximation is valid for only those data points near the cutoff frequency. We therefore studied the sensitivity of the fitted value of MOT cutoff frequency on the number of data points used for the fit, which is discussed in the next section.

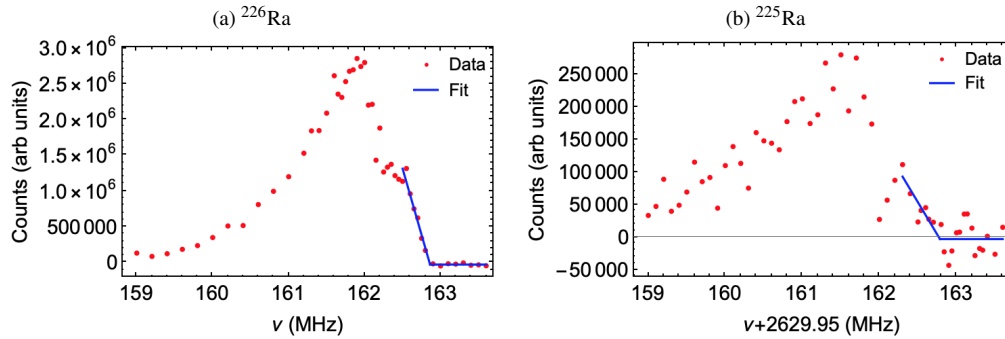


Fig. 8. Measured MOT fluorescence counts versus AOM frequency ( $\nu$ ) for (a)  $^{226}\text{Ra}$  and (b)  $^{225}\text{Ra}$ . The laser frequency for  $^{225}\text{Ra}$  is further offset from the cavity resonance relative to  $^{226}\text{Ra}$  by increasing the EOM offset frequency  $\Omega_1$  by 2629.95 MHz. The difference in the fluorescence counts of the two isotopes is primarily due to the different number of atoms loaded into the oven.

#### 4.4. Results and Discussion

The MOT fluorescence data for the two isotopes are shown in Fig 8. From the fits we determine the MOT cutoff frequency  $a_3$  for  $^{226}\text{Ra}$  (with statistical uncertainties) to be  $\nu_{226} = 162.862(20)$  MHz and for  $^{225}\text{Ra}$  to be  $\nu_{225} + 2629.95 \text{ MHz} = 162.785(102) \text{ MHz}$ . The frequency difference for the MOT transition between the two isotopes is therefore determined to be 2630.037 MHz with a statistical uncertainty of  $\sigma_{\Delta\nu, \text{stat}} = 0.104 \text{ MHz}$ .

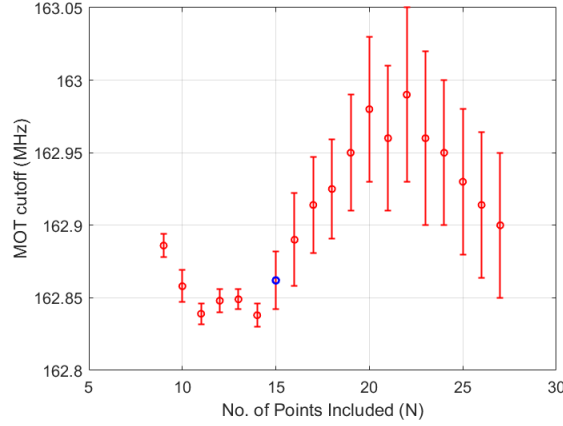


Fig. 9. MOT cutoff frequency  $a_3$  for  $^{226}\text{Ra}$  (probe power at 25.8 mW) as a function of the number of data points included in the fit, including the 8 last data points, up to the peak of the fluorescence spectrum. We fit the data up to the point before the MOT cutoff frequency value diverges by more than a standard deviation. In this case, for  $N$  greater than 15, the value of  $a_3$  diverges and so only up to the  $N = 15$  data point (blue data point) are included in the fit.

To select the number of data points to include in our fit, we study the effects of including certain number of data points on the fit values of MOT cutoff frequency  $a_3$ . For example, for our  $^{226}\text{Ra}$  dataset at 25.8 mW MOT probe power, we fit the dataset containing data points between the peak of the dataset and the eighth from the last data point and observe how the fit values for  $a_3$  changes. We expect the fit values for  $a_3$  to converge to the true value near the actual MOT cutoff frequency, where the linear approximation holds, and to diverge as we include more points and this approximation breaks down. As shown in Figure 9, the MOT cutoff frequency fit values diverge by more than one standard deviation after more than 15 data points are included in the fit. We therefore fit for the MOT cutoff frequency  $a_3$  using the last 15 data points for the above dataset. The data and the resultant fit is shown in Figure 8a. This method for determining the cutoff frequency is repeated for all the MOT cutoff datasets taken for  $^{226}\text{Ra}$  and  $^{225}\text{Ra}$ .

We study the potential systematic effects of MOT probe laser power and the MOT gradient B-fields on our MOT cutoff frequency determination in  $^{226}\text{Ra}$ . For the MOT probe power dependence, we keep the probe MOT gradient B-field constant and measure a MOT fluorescence spectrum at various probe laser powers. The dependence of the cutoff frequency on the MOT probe power for  $^{226}\text{Ra}$  is shown in Figure 10a. We estimate the size of this effect by using the largest possible difference in the MOT cutoff fit values from the four different MOT probe powers studied. This conservatively puts the effect at the level of 180 kHz.

Additionally, we investigate the effect of the MOT B-field gradient on the observed cutoff frequency by measuring MOT fluorescence spectra using different currents applied to the anti-Helmholtz MOT B-field coils during the probe phase. The plot of the MOT cutoff frequency fit values for the different MOT B-field coil currents are shown in Figure 10b. We similarly

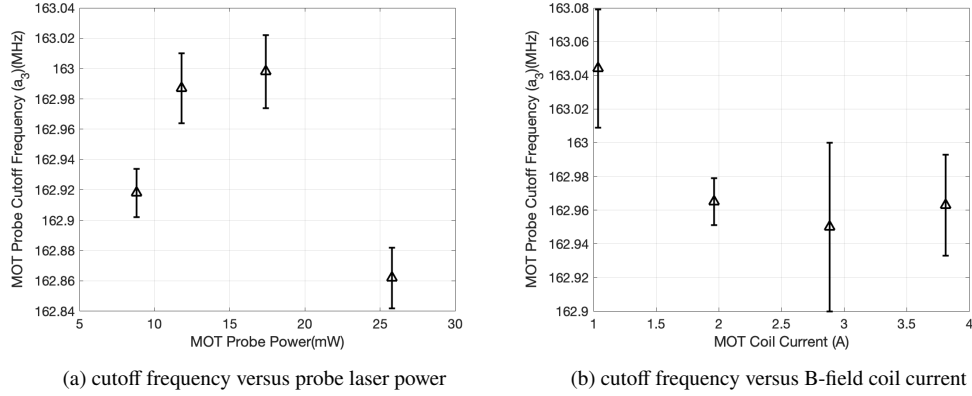


Fig. 10. The MOT cutoff frequency for  $^{226}\text{Ra}$  is plotted for different values of (a) MOT laser power and (b) MOT B-field coil current that are applied during the probe phase of the experimental cycle. Using the largest possible variation in MOT cutoff frequency for each systematic effect, we place a limit on the size of the effect.

estimate the size of this effect at 180 kHz. Cumulatively, adding in quadrature, the total systematic effect is  $\sigma_{\Delta\nu, \text{sys}} = 0.254$  MHz. Adding this in quadrature to the statistical uncertainty of  $\sigma_{\Delta\nu, \text{stat}} = 0.104$  MHz gives a total uncertainty on our MOT cutoff frequency difference between the two isotopes of  $\sigma_{\Delta\nu} = 0.274$  MHz. The frequency difference for the MOT transitions between  $^{226}\text{Ra}(^1S_0 \rightarrow ^3P_1)$  and  $^{225}\text{Ra}(^1S_0 [F=1/2] \rightarrow ^3P_1 [F=3/2])$  is therefore determined to be

$$\begin{aligned} \Delta\nu &= \nu_{226} - \nu_{225} \\ &= 2630.0 \pm 0.3 \text{ MHz} \end{aligned} \quad (6)$$

This is consistent with the value calculated from previously available spectroscopic data for radium [20] of  $2629.0 \pm 8.6$  MHz and is a factor of 29 more precise. Additionally, along with the known hyperfine splitting between the  $F = 1/2$  and the  $F = 3/2$  levels of  $^3P_1$ , we use our measurement of the difference in the MOT transitions between  $^{226}\text{Ra}$  and  $^{225}\text{Ra}$  to calculate the isotope shift  $\Delta\nu_{\text{iso}}$  between these two isotopes for the  $^1S_0$  to  $^3P_1$  transition:

$$\begin{aligned} \Delta\nu_{\text{iso}} &= \frac{1}{3} \Delta\nu_{\text{hfs}} - \Delta\nu \\ &= \frac{14691}{3} - 2630 \\ &= 2267.0 \pm 2.2 \text{ MHz} \end{aligned} \quad (7)$$

This is a factor of 8 more precise than the isotope shift of  $2268 \pm 17$  MHz that can be determined from Ref. [20]. It should be noted that, in Ref. [20], the isotope shifts for the  $^1S_0$  to  $^3P_1$  transition were measured for a range of radium isotopes with respect to  $^{214}\text{Ra}$ . Therefore it is possible that the uncertainty of 17 MHz propagated onto this isotope shift between  $^{226}\text{Ra}$  and  $^{225}\text{Ra}$  is overestimated. Since, to the best of our knowledge, no direct measurements of this isotope shift is reported, we take the above calculated value and its propagated uncertainty to be the currently best available measurement.

## 5. Conclusion

We have demonstrated the implementation of a broadband tunable ESB offset lock using an IQ modulation scheme. The ESB offset lock on our 483 nm ECDL1 laser is compared to a PDH lock on the same laser to characterize the ESB lock performance. We find that the noise level for the ESB lock is about 3 dB higher in the sub-MHz region compared to the PDH lock. In our 714 nm laser, we do not notice any significant changes in the laser frequency linewidth.

Suggestions for optimizing the ESB lock are provided. RAM in the system can introduce significant drifts in the error signal DC offset. Adjusting the EOM temperature and tuning the input polarization has been shown to be most effective in reducing RAM in our system. Photo refractive damage is a serious concern for short wavelength fiber EOMs such as our 714 nm phase modulator and an appropriate limit on the input optical power needs to be placed.

Using this highly tunable ESB offset laser frequency stabilization scheme, with a 714 nm laser locked to the same resonance of a ULE optical cavity, we determine the frequency shift required for the MOT transition frequencies between  $^{226}\text{Ra} ({}^1S_0 \text{ to } {}^3P_1)$  and  $^{225}\text{Ra} ({}^1S_0 [F = 1/2] \text{ to } {}^3P_1 [F = 3/2])$  to be  $2630.0 \pm 0.3$  MHz. Our measurement is a factor of 29 more precise than what can be calculated from the previously available spectroscopic data on radium. Using this measurement and the available hyperfine splitting in the  ${}^3P_1$  level in  $^{225}\text{Ra}$ , we determine the isotope shift for the  ${}^1S_0 \text{ to } {}^3P_1$  transition between  $^{226}\text{Ra}$  and  $^{225}\text{Ra}$  to be  $\Delta\nu_{\text{iso}} = 2267.0 \pm 2.2$  MHz. To the best of our knowledge, this is a factor of 8 better than the currently best available data and, as a consequence, the most precise measurement of this quantity.

The ESB locking technique used to obtain these results is broadly applicable to myriad physical systems to improve the precision of differential frequency measurements and could be expanded to frequency differences beyond 6 GHz through the use of a higher bandwidth IQ modulator. We expect this technique will significantly improve precision in isotope shift spectroscopy in particular, but could have broader impacts in laser spectroscopy more generally.

**Funding.** This work is supported by the U.S. DOE, Office of Science, Office of Nuclear Physics under contracts DE-AC02-06CH11357 and DE-SC0019455, and by Michigan State University.

**Acknowledgments.**

**Disclosures.** The authors declare no conflicts of interest

**Data Availability.** Data underlying the results presented in this paper are not publicly available at this time but may be obtained from the authors upon reasonable request.

## References

1. T. W. Hänsch and H. Walther, “Laser spectroscopy and quantum optics,” *Rev. Mod. Phys.* **71**, S242–S252 (1999).
2. W. D. Phillips, “Nobel lecture: Laser cooling and trapping of neutral atoms,” *Rev. Mod. Phys.* **70**, 721–741 (1998).
3. D. S. Jin and J. Ye, “Introduction to Ultracold Molecules: New Frontiers in Quantum and Chemical Physics,” *Chem. Rev.* **112**, 4801–4802 (2012).
4. L.-M. Duan and C. Monroe, “Colloquium: Quantum networks with trapped ions,” *Rev. Mod. Phys.* **82**, 1209–1224 (2010).
5. R. W. P. Drever, J. L. Hall, F. V. Kowalski, J. Hough, G. M. Ford, A. J. Munley, and H. Ward, “Laser phase and frequency stabilization using an optical resonator,” *Appl. Phys. B* **31**, 97–105 (1983).
6. E. D. Black, “An introduction to pound–drever–hall laser frequency stabilization,” *Am. J. Phys.* **69**, 79–87 (2001).
7. F. Bondu, P. Fritschel, C. N. Man, and A. Brillet, “Ultrahigh-spectral-purity laser for the virgo experiment,” *Opt. Lett.* **21**, 582–584 (1996).
8. J. Ye and J. L. Hall, “Optical phase locking in the microradian domain: potential applications to nasa spaceborne optical measurements,” *Opt. Lett.* **24**, 1838–1840 (1999).
9. J. I. Thorpe, K. Numata, and J. Livas, “Laser frequency stabilization and control through offset sideband locking to optical cavities,” *Opt. Express* **16**, 15980–15990 (2008).
10. R. Kohlhaas, T. Vanderbruggen, S. Bernon, A. Bertoldi, A. Landragin, and P. Bouyer, “Robust laser frequency stabilization by serrodyne modulation,” *Opt. Lett.* **37**, 1005–1007 (2012).
11. J. Bai, J. Wang, J. He1, and J. Wang, “Electronic sideband locking of a broadly tunable 318.6 nm ultraviolet laser to an ultra-stable optical cavity,” *J. Opt.* **19** (2017).

12. T. E. Chupp, P. Fierlinger, M. J. Ramsey-Musolf, and J. T. Singh, "Electric dipole moments of atoms, molecules, nuclei, and particles," *Rev. Mod. Phys.* **91**, 015001 (2019).
13. J. Dobaczewski and J. Engel, "Nuclear time-reversal violation and the schiff moment of  $^{225}\text{Ra}$ ," *Phys. Rev. Lett.* **94**, 232502 (2005).
14. Y. Singh and B. K. Sahoo, "Electric dipole moment of  $^{225}\text{Ra}$  due to  $p$ - and  $t$ -violating weak interactions," *Phys. Rev. A* **92**, 022502 (2015).
15. V. A. Dzuba, V. V. Flambaum, and S. G. Porsev, "Calculation of  $(p, t)$ -odd electric dipole moments for the diamagnetic atoms  $^{129}\text{Xe}$ ,  $^{171}\text{Yb}$ ,  $^{199}\text{Hg}$ ,  $^{211}\text{Rn}$ , and  $^{225}\text{Ra}$ ," *Phys. Rev. A* **80**, 032120 (2009).
16. N. Auerbach, V. V. Flambaum, and V. Spevak, "Collective  $t$ - and  $p$ -odd electromagnetic moments in nuclei with octupole deformations," *Phys. Rev. Lett.* **76**, 4316–4319 (1996).
17. M. Bishof, R. H. Parker, K. G. Bailey, J. P. Greene, R. J. Holt, M. R. Kalita, W. Korsch, N. D. Lemke, Z.-T. Lu, P. Mueller, T. P. O'Connor, J. T. Singh, and M. R. Dietrich, "Improved limit on the  $^{225}\text{Ra}$  electric dipole moment," *Phys. Rev. C* **94**, 025501 (2016).
18. P. Welch, "The use of fast Fourier transform for the estimation of power spectra: A method based on time averaging over short, modified periodograms," *IEEE Transactions on Audio Electroacoustics* **15**, 70–73 (1967).
19. W. Zhang, M. J. Martin, C. Benko, J. L. Hall, J. Ye, C. Hagemann, T. Legero, U. Sterr, F. Riehle, G. D. Cole, and M. Aspelmeyer, "Reduction of residual amplitude modulation to  $1 \times 10^{-6}$  for frequency modulation and laser stabilization," *Opt. Lett.* **39**, 1980–1983 (2014).
20. K. Wendt, S. A. Ahmad, W. Klempt, R. Neugart, E. W. Otten, and H. H. Stroke, "On the hyperfine structure and isotope shift of radium," *Z. Phys. D: At., Mol. Clust.* **4** (1987).